JAAS

PAPER

View Article Online
View Journal | View Issue

Cite this: J. Anal. At. Spectrom., 2026, 41, 1375

Lamb dip saturated cavity ring-down spectroscopy of gadolinium isotopes in a DC glow discharge

Ryohei Terabayashi, *[ab] Yuko Nojiri[a] and Shuichi Hasegawa*[a]

We demonstrate a cavity ring-down spectroscopy (CRDS) system using a direct-current (DC) hollow-cathode glow discharge plasma as an atomic source for isotope-resolved spectroscopy of gadolinium (Gd). This DC glow discharge CRDS provides a compact and simple alternative to conventional inductively coupled plasma (ICP)-based CRDS, while maintaining sufficient stability for high-sensitivity measurements. Saturation effects, more pronounced in atomic than molecular CRDS due to large absorption cross sections, were captured using a saturation model applied to ring-down transients. Saturated CRDS enabled clear observation of Doppler-free lamb dips in Gd spectra, highlighting its capability to resolve narrow spectral features. Combined analysis of Doppler-broadened absorption and lamb dip components allowed estimation of isotopic ratios for the even Gd isotopes, consistent with natural abundances, except for ^{155}Gd and ^{157}Gd. These results demonstrate the feasibility of applying saturated CRDS to precise isotope ratio measurements of rare-earth elements, and suggest the potential applicability of the technique to other metal atoms, including uranium, plutonium, and other transuranic elements.

Received 1st December 2025
Accepted 19th February 2026

DOI: 10.1039/d5ja00476d

rsc.li/jaas

1 Introduction

High-sensitivity absorption spectroscopy utilizing multiple reflections within an optical resonator is an effective technique for measuring trace substances in gaseous form.[1] Among these cavity-enhanced absorption spectroscopy, cavity ring-down spectroscopy (CRDS)[2] is known as one of the most sensitive techniques and has been widely applied to measure atmospheric molecules or their isotopologues.[3,4] In particular, the detection of radiocarbon dioxide ($^{14}CO_2$) using CRDS with sensitivities ranging from parts per trillion (ppt, 10^{-12}) to parts per quadrillion (ppq, 10^{-15}) demonstrates its capability for ultra-trace molecular spectroscopy.[5,6]

Applications of CRDS to metal elements have also been explored, where atomic absorption spectra are obtained by atomizing and evaporating target elements. For instance, ref. 7 reported absorption spectra of iron, aluminum, molybdenum, and titanium sputtered by an argon ion beam, and a CRDS system measuring electronic transitions of erbium isotopes from a tantalum crucible achieved a detection limit of 2×10^6 atoms per cm^3.[8] Various plasma sources have been implemented as atomic sources in CRDS (plasma-CRDS, P-CRDS).[9] Inductively coupled plasma (ICP)-CRDS was first demonstrated in 1997,[10] with uranium isotope spectra measured in 2003.[11] Subsequent reports on technological advances in this field have been limited.

Here, we present a CRDS system using a direct-current (DC) glow discharge plasma for isotope-resolved measurements of gadolinium. Compared with ICP, DC glow discharge plasmas require simpler electrical circuits and a single DC power supply, allowing for a more compact and portable setup.[12,13] Although lower plasma power may reduce atomization efficiency, the correspondingly lower plasma temperature can help suppress spectral broadening. A previous study demonstrated the use of DC glow discharge plasma in CRDS for xenon isotope measurements,[14] where the plasma mainly served to excite xenon atoms. In this work, we employed a hollow-cathode plasma cell to confine the plasma along the laser path, thereby improving the detection limit.

Gadolinium has seven naturally occurring isotopes: ^{52}Gd, ^{154}Gd, ^{155}Gd, ^{156}Gd, ^{157}Gd, ^{158}Gd, and ^{160}Gd. Its isotopic composition is relevant in various fields. In nuclear engineering, ^{155}Gd and ^{157}Gd act as burnable poisons in uranium fuels, and are used to study fission behavior.[15,16] Gadolinium isotopes are also studied in geoscience through neutron capture reactions and cosmic ray irradiation in planetary materials,[17,18] and in medicine for applications such as gadolinium neutron capture therapy (Gd-NCT) and MRI contrast enhancement.[19,20] Techniques for isotope separation or enrichment, including chromatography[21,22] and laser photoionization,[23,24] highlight the importance of gadolinium isotope analysis.

[a]Nuclear Professional School, The University of Tokyo, 2-22, Shirakata-Shirane, Tokai, Ibaraki, 319-1118, Japan. E-mail: terabayashi.ryouhei.e6@f.mail.nagoya-u.ac.jp; hasegawa@tokai.t.u-tokyo.ac.jp

[b]Department of Applied Energy, Nagoya University, Furo-cho, Nagoya, Aichi, 464-8603, Japan

Mass spectrometry techniques, including thermal ionization mass spectrometry (TIMS)[25] and multi-collector ICP-MS (MC-ICP-MS),[26] have been used for gadolinium analysis, providing accurate isotope ratios with standard samples. However, accuracy can be compromised by isobaric interferences. Resonance ionization mass spectrometry (RIMS) with multiple lasers[27] addresses these interferences but adds experimental complexity. CRDS offers a spectroscopic alternative.

Atomic absorption cross sections are several orders of magnitude larger than molecular ones, and high intracavity intensities readily induce absorption saturation, which limits the applicability of conventional CRDS. Under sufficiently strong saturation, counter-propagating laser fields can selectively interact with atoms whose velocity component along the laser propagation axis is zero, leading to a narrow reduction in absorption at the line center known as a lamb dip.[28] This Doppler-free feature enables spectral resolution beyond the Doppler width and is particularly advantageous for precise isotope and hyperfine structure measurements. While saturated CRDS models have been well developed for molecular species such as $^{14}CO_2$,[5,29] applications to atomic species remain limited. Lamb dip observations using saturated CRDS have been reported for molecular species,[30] while the first observation for an atomic species was reported in 2023 for the Balmer-α line of hydrogen.[31] More recently, Lamb dip CRDS has been applied to metastable neon (Ne*).[32]

In this study, we demonstrate saturated CRDS for gadolinium isotopes in a DC glow discharge, report Doppler-free lamb dip observations, and derive isotope ratios evaluated from these spectra. To the best of our knowledge, this work represents the first demonstration of saturated and Doppler-free lamb dip CRDS applied to heavy metal isotopes such as Gd.

2 Principal of DC glow discharge CRDS and saturated CRDS

2.1. DC glow discharge CRDS

Cavity ring-down spectroscopy (CRDS) employs a highly reflective optical resonator to enhance the effective optical path length, increasing absorption sensitivity. Unlike conventional absorption spectroscopy, CRDS measures the decay time constant of photons stored in the cavity rather than the transmitted laser power. When laser photons satisfy the cavity resonance condition, they accumulate in the resonator; after rapid shut-off of the injected laser, the transmitted intensity decays due to intracavity losses. For a Fabry–Perot cavity composed of two mirrors, the transmitted intensity $I(t)$ is expressed as:[34]

$$I(t) = I_0 \exp\left(-\frac{t}{\tau}\right) \tag{1}$$

where I_0 is the initial intensity and τ is the ring-down time constant. For conventional CRDS, where losses are dominated by mirror reflectivity and sample absorption, τ is expressed as:

$$\tau = \frac{L}{(1-R)c + \alpha(\nu)Lc} \tag{2}$$

with L the cavity length, R the average mirror reflectivity, c the speed of light, and $\alpha(\nu)$ the sample absorption coefficient at frequency ν. The corresponding ring-down rate is $\beta = 1/\tau$, from which the sample absorption can be derived.

$$\beta = \frac{(1-R)c}{L} + \alpha(\nu)c \tag{3}$$

In plasma-based CRDS, additional optical losses from scattering in the plasma and non-plasma regions must be considered:[33]

$$\tau = \frac{L}{(1-R)c + \beta_{\text{plasma}} lc + \beta_{\text{gas}}(L-l)c + \alpha(\nu)cl} \tag{4}$$

where β_{plasma} and β_{gas} are scattering coefficients in the plasma and non-plasma regions, respectively, and l is the laser path length through the plasma. By including all non-sample losses in a reference ring-down rate $\beta_0^{'}$, the absorption coefficient is obtained as:

$$\alpha(\nu) = \sigma(\nu)N = \frac{L}{lc}\left(\beta - \beta_0^{'}\right) \tag{5}$$

where N and $\sigma(\nu)$ denote the absorber number density and absorption cross section, respectively. Although σ and N may vary radially due to plasma inhomogeneity,[34] the spatially averaged value should be sufficient for isotope analysis demonstrated in this paper.

The absorption cross section for a transition from lower state i to upper state j is:[35]

$$\sigma_{ij}(\nu) = \frac{c^2}{8\pi\nu^2}\frac{g_j}{g_i}A_{ji}f(\nu) \tag{6}$$

where $g_{j,i}$ are state degeneracies, A_{ji} is the Einstein A coefficient, and $f(\nu)$ is an area-normalized line-shape function. Spectral broadening is described using a Voigt profile $V(\nu, \nu_0, \Delta\nu_D, \Delta\nu_L)$, a convolution of Gaussian (Doppler) and Lorentzian components, with Doppler width[36]

$$\Delta\nu_D = \frac{\nu_0}{c}\cdot\sqrt{\frac{8k_B T\cdot\ln 2}{m}} \tag{7}$$

where k_B is the Boltzmann constant, T the temperature of the atoms (~1000 K in DC glow plasma), and m the atomic mass.

For multiple absorption peaks, the total absorption is modeled as a sum of isotopic contributions plus background $C_{BG}(\nu)$:

$$F(\nu) = \sum_k A_k\ V(\nu,\ \nu_{0\_k},\ \Delta\nu_{D\_k},\ \Delta\nu_{L\_k}) + C_{BG}(\nu) \tag{8}$$

where k indexes each isotopic absorption peak and $A_k = N_k\sigma_k$ represents the corresponding absorption amplitude. Regarding $C_{BG}(\nu)$, it may be frequency-independent, however, etaloning and spurious reflections[37] introduce oscillatory background, which can be modeled using polynomial, sinusoidal, Airy functions, or their combinations. Assuming σ_k is the same for all isotopes, eqn (8) can be rewritten as:

$$F(\nu) = A\sum_k r_k\ V(\nu, \nu_{0\_k}, \Delta\nu_{D\_k}, \Delta\nu_{L\_k}) + C_{BG}(\nu) \tag{9}$$

here r_k denotes the isotopic abundance ratio and A represents the total amplitude term. Multi-Voigt fitting thus allows estimation of A, $C_{BG}(\nu)$, and (r_k, ν_{0_k}, $\Delta\nu_{D\_k}$, $\Delta\nu_{L\_k}$). The atomic number density is then calculated from:

$$N_k = \frac{A_k}{\sigma_k} = \frac{A\ r_k}{\frac{c^2}{8\pi\nu^2}\frac{g_j}{g_i}A_{ji}} \tag{10}$$

For Gd analysis, $\Delta\nu_{Dk}$ and $\Delta\nu_{Lk}$ were assumed equal among isotopes, except for ^{155}Gd and ^{157}Gd due to their hyperfine structures (HFS).[38] For these two isotopes, the centroid frequencies $\nu_{0,155}$ and $\nu_{0,157}$ were used, treated as individual Voigt components with broadened profiles differing from the even isotopes. In this approach, r_{155} and r_{157} serve as empirical scaling factors for the centroid intensities and cannot be interpreted directly as isotopic abundance ratios. This treatment is valid only when HFS components are spectrally unresolved due to limited spectral resolution.

2.2. Saturated CRDS

Absorption saturation occurs when continuous optical pumping depletes the population of the lower state contributing to absorption. In CRDS, the degree of saturation varies over time due to the decay of intracavity light intensity, causing the ring-down signal to deviate from the simple exponential behavior of eqn (1). Galli *et al.* modeled these transient dynamics and proposed saturated CRDS.[39] This approach allows separate evaluation of the decay rate in the absence of absorption (background, γ_c) and the decay rate associated with unsaturated absorption (γ_g), corresponding to $(1-R)c/L$ and $\alpha(\nu)c$ in eqn (3), respectively. This method has enabled ppq-level sensitivity in $^{14}CO_2$ analysis.

Several variants of saturated CRDS have been reported; in this study, we adopted the model for inhomogeneously broadened absorption from ref. 40:

$$S(t) = S_0\exp(-\gamma_c t) f(t, \gamma_c, \gamma_g, Z^{1V}) \tag{11}$$

$$\frac{df(t)}{dt} = -\frac{2\ \gamma_g\ f(t)}{1+\sqrt{1+S_0 Z^{1V}\exp(-\gamma_c\ t)f(t)}} \tag{12}$$

here, $S(t)$ is the observed ring-down transient measured by a photodetector, S_0 is the initial amplitude at $t = 0$, and Z^{1V} denotes the saturation level at $t = 0$, corresponding to a signal amplitude of 1 V. As Z^{1V} increases, the absorption medium approaches transparency due to saturation effects. In conventional CRDS, the ring-down signal is fitted using eqn (1) through regression analysis to estimate the decay rate. In contrast, in saturated CRDS, fitting is performed using eqn (11) to estimate both γ_c and γ_g. In this case, the transient saturation behavior described by $f(t)$ requires numerical integration of eqn (12) to obtain the optimal solution, with the initial condition of $f(0) = 1$. In this study, a Python-based solver (solve_ivp, SciPy) was employed in combination with the regression fitting library (Lmfit). The parameters used in the fitting procedure were γ_c, γ_g, S_0, Z^{1V} and the detector DC offset: V_{offset}.

3 Experimental setup

Fig. 1 shows a schematic of the prototype spectrometer: (a) the optical layout of the probe laser, (b) the CRDS optical cavity and gas cell, and (c) the hollow-cathode glow-discharge plasma cell.

A self-assembled external cavity diode laser (ECDL) in a Littrow configuration[41] was employed as the probe laser. Its wavelength was tuned to ~422.6 nm to match the $4f^7 5d6s^2\ ^9D_6$ (1719.087 cm^{-1}) → $4f^7 5d6s6p\ ^9F_7$ (25 376.313 cm^{-1}) transition of gadolinium.[27] After an optical isolator, part of the light was sent to a wavemeter (High Finesse, WS-7), while the main beam was directed to an acousto-optic modulator (AOM, Isomet M1212-aQ200–0.8) acting as an optical switch. The first-order diffracted beam, with power adjusted by a $\lambda/2$ plate, was coupled into a polarization-maintained (PM) fiber and injected into the optical cavity *via* a mode-matching lens.

A $\lambda/2$ plate, polarization beam splitter cube (PBSc), and $\lambda/4$ plate suppressed reflections into the ECDL and allowed for potential future Pound–Drever–Hall (PDH) locking.[42] A UV-enhanced silicon photodetector with a low-noise transimpedance amplifier detected the transmitted light. The AOM was switched off immediately when the transmitted signal exceeded a comparator threshold, generating the ring-down signal, which was recorded using a high-resolution digitizer (National Instruments PXI-5922).

The gas cell consisted of a high-finesse optical cavity with a Duran glass NW40 cross at the center and stainless steel chambers on either side. Each end flange supported a pair of ultra-high reflectivity concave cavity mirrors (Layertec, R > 99.98%, rear surface AR-coated) mounted on 2-axis flexure mounts. The cavity length (~460 mm) was tuned across one free spectral range (FSR) using piezo actuators. Invar rods minimized thermal expansion caused by the glow discharge. Wedged optical windows allowed laser input/output.

Two types of gas inlets were installed: side ports for cavity mirror protection gas and a central port for plasma carrier gas and cathode flushing. Pure argon at 0.1 L per min per inlet was used, resulting in a cell pressure of ~300 Pa. Other noble gases, such as helium, are also feasible. A dry scroll pump continuously evacuated the cell.

The hollow-cathode plasma cell was modified from our previous design[12,13] for more uniform plasma and reduced impurity effects. Symmetric titanium components were used, except for ceramic insulators, copper anode wire, and stainless steel mounting rods. The inner hollow cathode tube (4.1 mm ID × 25 mm length) is removable for maintenance. The central titanium tube serves as the electrode and gas inlet, designed for future online sample injection similar to LA-GD-MS[43] or LA-ICP-MS.[44] The plasma circuit included a DC power supply (Texio PSW360-800H) and a 2 kΩ ballast resistor to ensure stable discharge.

Laser frequency scanning was achieved by locking the ECDL to a setpoint *via* the wavemeter and piezo feedback. By combining discrete setpoint adjustments with laser current modulation, the mode-hop-free range was extended, enabling continuous frequency sweeps exceeding 20 GHz at 422.6 nm.

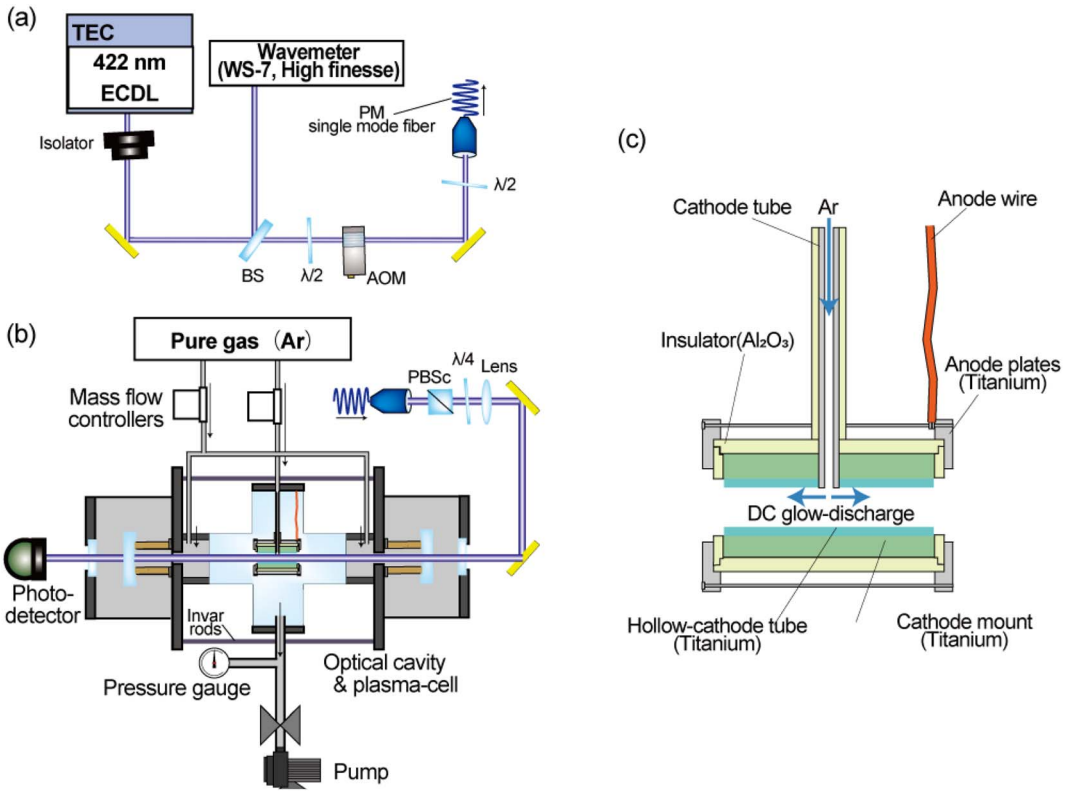

Fig. 1 Schematic of the experimental setup: (a) optical layout of the ECDL system, (b) gas cell incorporating the optical cavity and glow-discharge plasma cell, and (c) schematic of the hollow-cathode glow-discharge cell.

The scanning process was controlled using LabVIEW *via* a 16-bit USB DAQ board (Measurement Computing, USB-1808X), with frequency steps of 25 MHz s^{-1} and a total sweep time of ~800 s to allow sufficient averaging at each point of the CRDS spectra.

For Gd isotope spectroscopy, a small fragment of pure Gd thin plate (2.7 mg, 0.05 mm thickness, ~1 × 8 mm^2) was placed at the hollow cathode center, and the cell was evacuated. Argon was introduced from both ends and through the cathode.

4 Results and discussion

4.1. Noise analysis

In preparation for the spectral measurements, we investigated the effect of the DC glow discharge, generated at the center of the optical cavity, on the sensitivity of the CRDS system.

Fig. 2 shows the monitored CRD decay rate in response to power injection into a blank glow discharge cell, with stepwise increases in discharge current at a fixed laser frequency. The discharge was initially turned on at 5.3 W (20 mA), 50 s after the start of the recording, and subsequently increased to 10.4 W (40 mA) and 16.5 W (60 mA) at 100 s intervals.

Two types of background changes were observed. The first type, gradual changes beginning after the start of the discharge, is likely caused by thermal fluctuations. Equilibrium was reached in ~200 s, after which no significant variations were observed under stable conditions. The second type, rapid changes occurring immediately after each power step, is likely due to additional light losses caused by plasma-generated particles, *e.g.*, scattering effects as described in eqn (4).

Fig. 3 shows that this additional loss (background increase) scales linearly with the applied power, supporting the

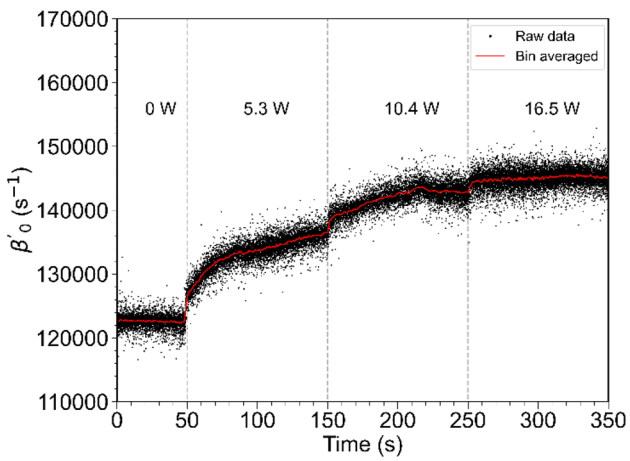

Fig. 2 Background ring-down decay rate monitoring during DC glow-discharge operation. The gray dashed lines indicate the times when the discharge injection power was increased. Two types of background changes were observed: a slow relaxation toward steady state reaching equilibrium in ~200 s after discharge ignition, and step-like rapid jumps in the decay rate occurring within a few seconds following changes in the discharge power.

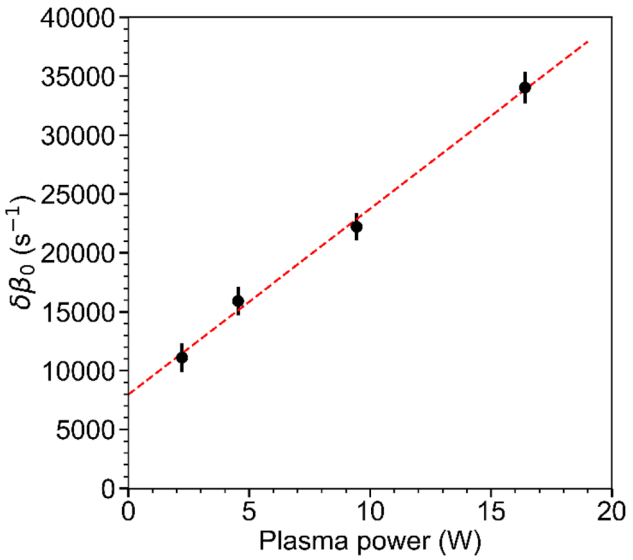

Fig. 3 Background increase as a function of discharge injection power. The *y*-axis shows the increase in the background decay rate relative to the discharge-off condition. The red dashed line represents a linear fit. Each point indicates the mean background increase, with error bars showing the standard deviation calculated from 10^4 measurements after sufficient stabilization time following each power change.

assumption that the number of generated particles increases with power. Importantly, no laser frequency-dependent background was observed over the scanning range, indicating that the plasma does not introduce spurious absorption features.

Fig. 4 presents a noise analysis based on the Allan–Werle plot for the same dataset as in Fig. 3. Despite the background increase caused by the DC glow discharge, the noise level of the CRDS system remained largely unaffected at applied powers up to 16.4 W, with only a slight deterioration in the averaging time due to increased system errors. These results suggest that low-power DC glow discharge has minimal impact on CRDS measurements. In addition, further reductions in noise could be achieved by employing mirrors with higher reflectivity in the UV range.

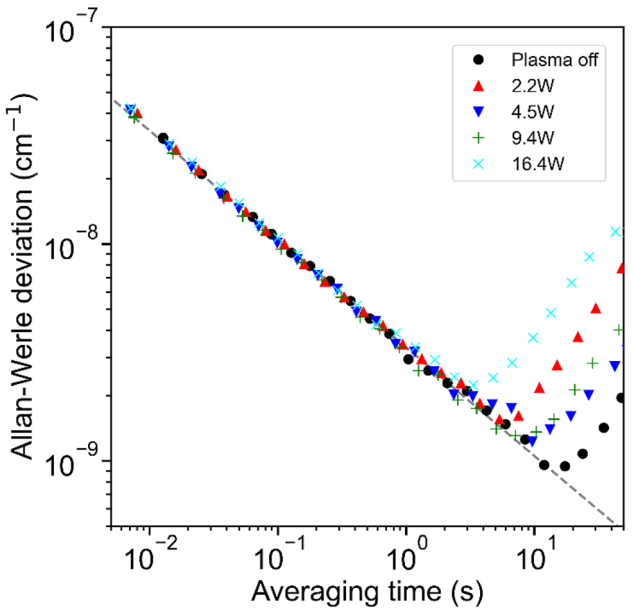

Fig. 4 Noise analysis based on the Allan–Werle plot. The dashed line shows the trend of the inverse square-root dependence on the number of averaged samples.

4.2. Saturated ring-down analysis

Fluctuations in the initial ring-down intensity directly influence the initial saturation level, presenting a major challenge for saturated-signal analysis. In this study, PDH locking was not employed, so variations in the coupling efficiency between the ECDL and the optical cavity dominated, leading to initial intensity fluctuations exceeding 50%. To address this, only traces with relatively high and stable saturation levels were selected and averaged to produce a representative trace for each frequency point. Specifically, for each frequency, traces were retained if their initial intensity exceeded the mean plus half the standard deviation of the full set (≈100 traces per point), effectively using the top ~30% of traces in terms of intensity. Implementing PDH locking is expected to greatly improve both intensity stability and statistical precision, and work toward this enhancement has already begun in our system.

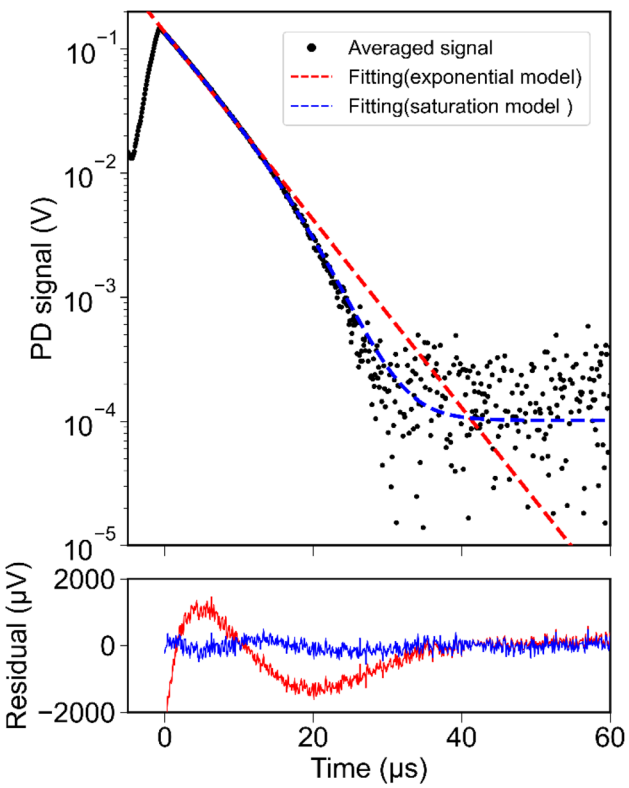

Fig. 5 Ring-down signal exhibiting a strong saturation effect (top) and corresponding fit residuals (bottom). Black dots denote the averaged experimental data; the blue curve represents the fit using the saturated ring-down model, while the red curve shows the fit using the conventional exponential CRDS model.

Fig. 5 shows a ring-down trace exhibiting saturation due to Gd atomic absorption, along with fits using both the conventional exponential CRDS model and the saturation model. The measured signal clearly deviates from a single exponential decay, whereas the saturation model successfully reproduces the transient behavior. A small oscillatory component remains in the residuals of the saturation-model fit, which may arise from a nonlinear detector response. As discussed in ref. 29, this could be accounted for by introducing a frequency-independent nonlinearity term into the saturation model. However, incorporating such a complex extension would reduce the reliability of parameter estimation and was therefore not pursued here. For future applications requiring higher sensitivity, such as trace isotope analysis, improvements in detector linearity combined with such model extensions may become necessary.

When the analysis illustrated in Fig. 5 was applied to the entire set of Gd isotope spectra, the results did not converge reliably if Z^{1V} was left as a free parameter. This issue arises from correlations between Z^{1V} in the denominator and γ_g in the numerator of eqn (12). Indeed, manually increasing Z^{1V} caused no significant change in χ^2, but the estimated γ_g increased accordingly. Consequently, the optimal value of Z^{1V} could not be determined solely from χ^2 minimization. Since Z^{1V} correlates with the absolute value of γ_g, its appropriate determination is essential for reliable comparisons.

To address this, we focused on the late part of the ring-down decay—several microseconds before the noise floor—and fitted this region with a simple exponential model. Although the associated uncertainties are large, this procedure provided a preliminary estimate of the absorption contribution using conventional CRDS, assumed to be unaffected by saturation. In the subsequent full-range saturation-model analysis, Z^{1V} was then fixed at 2000, a value that produced γ_g spectra consistent with the preliminary estimated absorption spectrum. Because absorption cross sections are expected to be nearly identical among isotopes for the same electronic transition, a common value of Z^{1V} can, in principle, be applied to all isotope measurements performed with the same setup and initial ring-down amplitude conditions. Fig. 6 shows an example of the decay rates obtained in the Gd isotope spectral measurements. The results labeled "Exponential" correspond to decay rates evaluated without considering saturation effects.

Another issue apparent in Fig. 6 is the coupling between the gas absorption rate (γ_g) and the cavity loss rate (γ_c), which manifests as negative peaks in γ_c. As noted in ref. 40, this effect begins to appear when $\gamma_g/\gamma_c > 1$, and the present results are consistent with that observation. While applications of saturated CRDS to molecular spectroscopy typically involve weak absorptions from trace molecules, atomic spectroscopy, as studied here, features several orders of magnitude larger absorption cross sections. Consequently, this coupling effect is more pronounced and may introduce γ_c-related uncertainties into analyses of γ_g-derived absorption spectra. Future work will explore a wider range of sample amounts to investigate the mechanism of this coupling and possible mitigation strategies. In summary, the established saturated CRDS model is suitable for atomic spectroscopy, but challenges in Z^{1V} estimation and γ_c–γ_g coupling indicate the need for further studies under varied conditions to develop a more universally applicable analytical methodology.

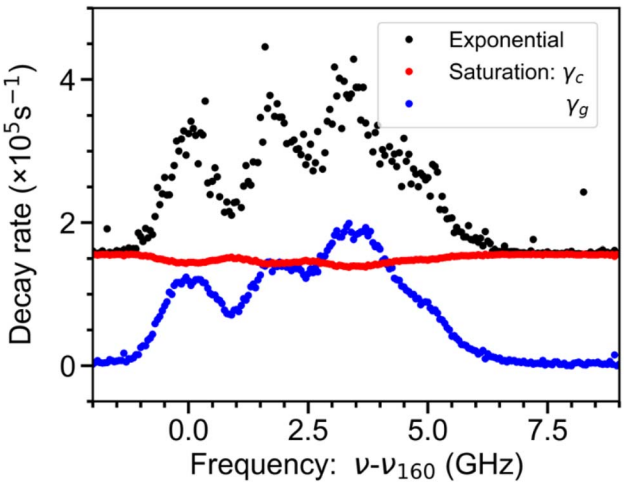

Fig. 6 Comparison of decay rates from the exponential model (black) and the saturation model (red: γ_c, blue: γ_g) at 2.1 W. The x-axis shows frequency relative to the ^{160}Gd peak center.

In summary, while the established saturated CRDS model proves suitable for atomic spectroscopy, the challenges associated with Z^{1V} estimation and γ_c–absorption coupling clearly indicate the need for further studies under varied conditions to develop a more universally applicable analytical methodology.

4.3. Gadolinium isotope spectroscopy

Isotope-resolved spectroscopy of gadolinium (Gd) was demonstrated using CRDS. Gd has seven stable isotopes (^{160}Gd, ^{158}Gd, ^{157}Gd, ^{156}Gd, ^{155}Gd, ^{154}Gd and ^{152}Gd) with natural abundance is 21.86(3)%, 24.84(8)%, 15.65(4)%, 20.47(3)%, 14.80(9)%, 2.18(2)% and 0.20(3)% respectively, according to the IUPAC technical report.[45] The target transition of Gd atom adopted in this paper was the $4f^75d6s^2\ ^9D_6$ (1719.087 cm^{-1}) → $4f^75d6s6p\ ^9F_7$ (25 376.313 cm^{-1}) at 422.6 nm, with the Einstein A coefficient of 8.9×10^7 s^{-1}.[46] Reported isotope shifts relative to ^{160}Gd are 1769.7(12) MHz, 3176.4(21) MHz, 3470.8(14) MHz, 4648.5(15) MHz, 5770.2(16) MHz and 11 093.1(18) MHz, for ^{158}Gd through ^{152}Gd, respectively.[47] For the odd-isotopes (^{157}Gd and ^{155}Gd), the listed values correspond to the center of gravity (cg) of the HFS peaks.

Fig. 7 shows a representative saturated-CRDS spectrum of Gd isotopes recorded at 5.4 W excitation power and a discharge current of 25 mA. Although the ~1.4 GHz Doppler width leads to partial overlap among peaks, contributions from all isotopes were successfully resolved. Clear lamb dips appear at the peak centers; therefore, the fitting model in eqn (9) was modified by adding negative Lorentzian terms at each transition frequency to represent the lamb dip components. For simplicity, the Lorentzian contributions were implemented by reducing the Doppler width parameter in the Voigt profile to a minimal value within the same functional form. Fig. 8 shows the extracted lamb dip components. In practice, both the Doppler-broadened

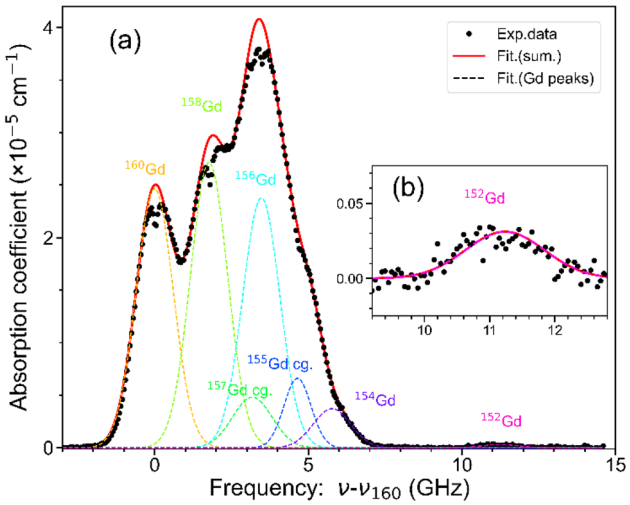

Fig. 7 Saturated CRDS spectrum obtained from a Gd metal plate under a 5.4 W (25 mA) glow discharge: (a) full frequency range and (b) enlarged view of the ^{152}Gd peak region. Black dots denote the experimental data; the solid curve represents the sum of fitted Voigt profiles for all Gd isotopes, and the dashed curves correspond to individual isotopic components. The *x*-axis represents the frequency relative to the center of the ^{160}Gd peak.

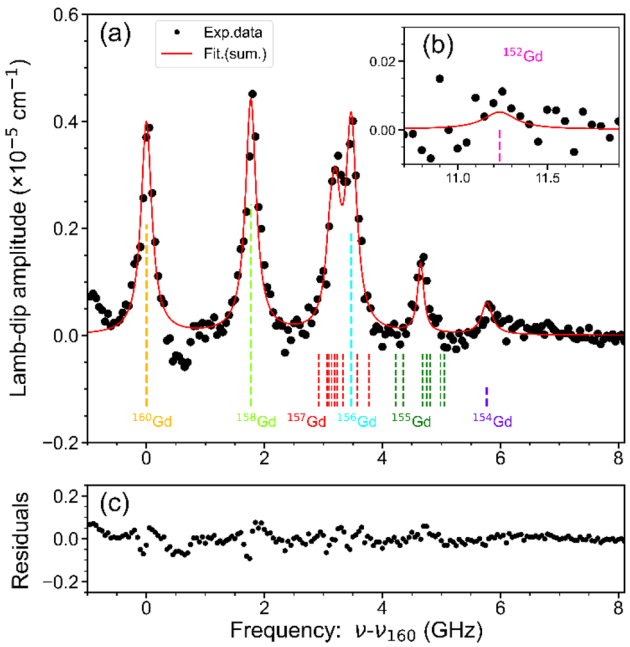

Fig. 8 Lamb dip spectrum derived from the residuals in Fig. 7 under a 25 mA discharge. Frequency is referenced to the ^{160}Gd peak. (a) ^{160}Gd–^{154}Gd region; (b) enlarged ^{152}Gd region; (c) residuals of the simultaneous fit. Black dots represent the experimental data; the solid curve represents the sum of fitted Lorentzian profiles; and the dashed vertical lines denote the individual Gd peak positions.

spectrum (Fig. 7) and the lamb dip spectrum (Fig. 8) were fitted simultaneously *via* nonlinear least-squares optimization. The residuals of the simultaneous fit are shown in Fig. 8(c), indicating that the overall agreement between the model and the experimental data is satisfactory over the spectral window. The natural linewidth (FWHM) calculated from the Einstein A coefficient is 14.2 MHz, whereas the observed lamb-dip FWHM of ~220 MHz is ≈15.5 times larger, consistent with strong power broadening due to the high intra-cavity power (see ref. 32 for a detailed discussion). Under these broadened conditions, the hyperfine components of the odd-isotopes remain unresolved even in the lamb dip spectrum; thus, their cg positions were used, and the corresponding line-width parameters were treated as independent free parameters, separate from those of the even-isotopes. Regarding absorption amplitudes, all isotopes shared a single overall intensity parameter A, corresponding to the Gd atomic number density, while isotopic fractions r_k were left as free parameters. The lamb dip amplitudes A_{lamb} were fitted independently, with isotopic ratios constrained to those obtained from the Doppler-broadened spectrum.

The applied discharge power gradually decreased to 5.4 W, 4.4 W, 3.2 W, 2.6 W, and 2.1 W, and spectra were recorded and analyzed in the same manner at each condition. The resulting Gd isotopic ratios are summarized in Table 1. The least abundant isotope, ^{152}Gd, could not be detected below 2.6 W, as its signal was buried in noise. It should also be noted that, for ^{155}Gd and ^{157}Gd, the fitted parameters r_{155} and r_{157} do not represent true isotopic abundances but rather serve as correlation coefficients due to unresolved HFS. The Doppler-broadened absorption profile and the narrow lamb dip features, excluding the odd-isotopes.

To quantitatively assess the isotopic-ratio estimation performance, we evaluate (i) the relative deviation $\delta = (r_k - r_k^{\mathrm{nat}})/r_k^{\mathrm{nat}}$ from the natural isotopic abundance and (ii) the relative standard deviation (RSD) of the measured ratios. Because the number of repeated measurements was limited ($N = 5$), the standard deviation is used to characterize the repeatability of individual measurements, rather than the standard error of the mean.

For ^{155}Gd and ^{157}Gd, the isotopic ratios were determined with good accuracy and precision: the relative deviations from the natural abundances were +3.2% for ^{160}Gd and −1.3% for ^{158}Gd, while the corresponding RSD values were on the around 3%. In contrast, the isotopic ratio estimates for ^{156}Gd, ^{154}Gd, and ^{152}Gd exhibited relatively large RSDs and less reliable δ values. This degradation in precision and accuracy is mainly attributed to spectral interference from nearby unresolved HFS transitions of the odd isotopes. In addition, for ^{152}Gd, the low natural abundance resulted in a weak absorption signal, further deteriorating the reliability of the isotopic ratio determination.

For comparison, the isotopic composition of gadolinium has been determined with sub-percent precision by MC-ICP-MS, which represents the current state-of-the-art technique for high-accuracy isotopic analysis. According to ref. 25, in MC-ICPMS measurements of the GADS-1 reference material, the isotope amount ratio $R_{160/158} = 0.87910(60)_{(k=1)}$ has been reported, corresponding to a relative uncertainty of 0.07%.

Further improvements in accuracy and precision of the present method will require measurements using reference materials (like the GADS-1) with well-characterized Gd isotopic

Table 1 Gd isotopic ratios estimated from saturated CRDS spectra[a]

	r_{160} (%)	r_{158} (%)	r_{157} (%)	r_{156} (%)	r_{155} (%)	r_{154} (%)	r_{152} (%)
Natural abundance[45]	21.86(3)	24.84(8)	15.65(4)	20.47(3)	14.80(9)	2.18(2)	0.20(3)
5.4 W (25 mA)	23.07(6)	25.42(9)	4.75	22.28(29)	4.93	3.47(11)	0.29(5)
4.4 W (20 mA)	22.52(5)	24.33(5)	5.04	18.59(20)	4.86	2.17(5)	0.22(4)
3.2 W (15 mA)	21.50(5)	23.99(8)	4.64	19.52(23)	4.23	3.06(8)	0.20(5)
2.6 W (12 mA)	21.52(7)	24.21(10)	4.68	19.85(31)	4.28	3.04(11)	ND*
2.1 W (10 mA)	22.18(14)	24.65(20)	4.46	20.45(64)	4.46	2.91 (27)	ND*
Mean (SD)	22.56(59)	24.52(81)	—	20.54(153)	—	2.97(12)	0.24(3)

[a] ND: not detected.

compositions, as well as systematic optimization of experimental parameters. Such efforts represent an important subject for future work toward establishing this method for rapid and *in situ* isotopic analysis.

The estimated Doppler widths (FWHM) were 1.43 GHz at the maximum applied power of 4.4 W and 1.28 GHz at the minimum power of 2.1 W, showing a linear decrease with decreasing power. Similarly, the neutral Gd temperature derived from the modified form of eqn (7) exhibited a corresponding linear dependence on the discharge power (Fig. 9), indicating that the sputtering and thermalization processes remained in a steady glow-discharge regime without noticeable transitions in plasma conditions. Because the intra-cavity laser beam diameter ($\approx$0.4 mm, $1/e^2$) was much smaller than the inner diameter of the hollow cathode (4.1 mm) and aligned approximately along its central axis, the measured Doppler widths primarily reflect the kinetic temperature of ground-state neutral Gd atoms stably present in the bulk plasma region.

In the present study, a solid Gd metal target was employed, for which no time-dependent reduction in atomic density was observed, enabling stable and extended measurements. It should be noted, however, that the achievable measurement duration may vary significantly depending on the sample form, composition, and analyte inventory, and could be limited for samples prone to depletion.

In such cases, higher time-resolution spectral acquisition would be required. With further refinement of the measurement protocol and ring-down acquisition scheme, CRDS can capture transient variations in the atomic number density while maintaining reliable spectroscopic performance.

Based on the stable operating conditions established in the present study, using A and r_{160}, the atomic number density of ^{160}Gd was calculated from eqn (10). The dependence of the ^{160}Gd atomic number density on the applied power is shown in Fig. 10. It is empirically known that the atomic sputtering rate S in a DC glow discharge, often follows a linear dependence on the applied power, expressed as $S \propto k(P - P_0)$, where k and P_0 are

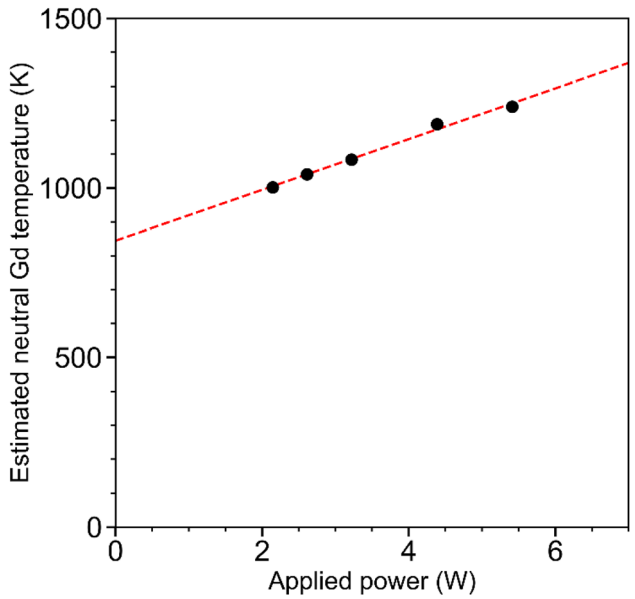

Fig. 9 Power dependence of the neutral Gd temperature estimated from the Doppler width obtained by spectral fitting. The dashed line indicates the linear trend. The standard deviations (0.3–1.0%) are smaller than the symbol size and are therefore not visible.

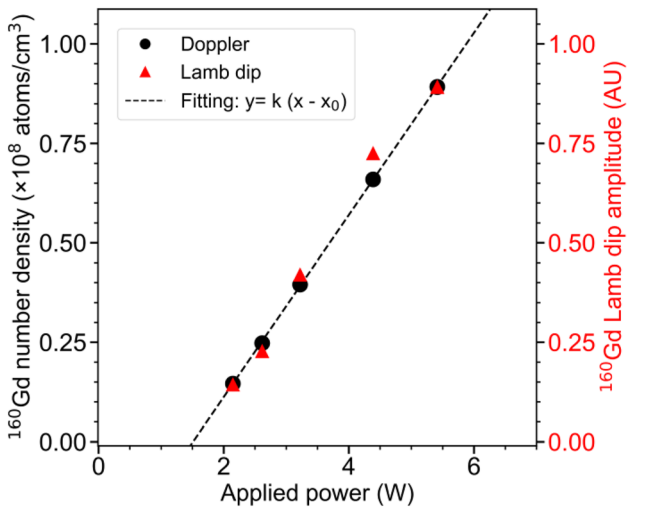

Fig. 10 Correlation between the applied power and the atomic number density of ^{160}Gd estimated from Doppler-broadened spectral fitting (black dots) and the ^{160}Gd lamb dip amplitude obtained from Lorentzian fitting (red triangles). The standard deviations (0.5–1%) are smaller than the symbol size and are therefore not shown. The dashed line represents a linear fit to the Doppler-based data.

constant.[48] The present experimental results agree well with this empirical relationship.

For the lamb dip amplitude A_{lamb}, normalization was performed so that the result at 5.4 W coincides with the calculated atomic number density. The power dependence of the normalized A_{lamb} showed good agreement with that of the estimated atomic number density, as indicated by the red triangles in Fig. 10. This consistency suggests that the lamb dip amplitude can also serve as a quantitative probe for monitoring variations in the Gd atomic number density within the plasma cell.

Finally, the sensitivity of the present system was evaluated in terms of the noise-equivalent detection limit of the atomic number density. Based on the measurement condition where ^{152}Gd could be detected at 3.2 W, the detection limit was estimated to be approximately 3×10^5 atoms per cm^3. Assuming that the plasma volume is equivalent to the cathode tube volume (0.33 cm^3) and that the atoms are uniformly distributed within this volume, the minimum detectable number of ^{152}Gd atoms corresponds to 1×10^5 atoms. For reference, compared with the reported detection limit of a CRDS system for Er atoms,[8] the present system demonstrates a sensitivity approximately one order of magnitude higher, clearly highlighting the excellent spectroscopic performance of the developed setup.

5 Conclusion

In this study, we developed and demonstrated a cavity ring-down (CRD) spectrometer employing a direct-current (DC) hollow-cathode glow discharge plasma as the atomic source and applied it to isotope-resolved spectroscopy of gadolinium (Gd). Compared with inductively coupled plasma-based CRDS, the DC glow discharge approach offers simpler operation and a more compact system design, while maintaining sufficient stability for high-sensitivity measurements.

Noise characterization confirmed that the low-power DC glow discharge minimally impacts CRDS sensitivity, and applying a saturation model enabled reliable observation of Doppler-free features in Gd spectra. Using combined Doppler-broadened and lamb dip analysis, saturated CRDS provided precise isotopic ratios for stable Gd isotopes.

Although the accuracy and precision achieved in the present study are lower than those attainable by state-of-the-art techniques such as MC-ICPMS, which provide sub-percent-level precision, the results demonstrate that Gd isotopic ratio estimation with relative deviations on the order of a few percent can be achieved without isotopic normalization or ultra-high-vacuum instrumentation. Toward practical analysis of real samples, further efforts based on the present results—particularly systematic optimization and calibration using reference materials with well-characterized Gd isotopic compositions—will be essential for improving both accuracy and precision.

From an instrumentation perspective, additional gains in sensitivity and precision are expected if ultra-high-reflectivity cavity mirrors (>99.995%), already available in the visible and infrared spectral regions, can be extended to ultraviolet wavelengths.

Importantly, the present approach enables sub-Doppler spectral resolution and isotopic discrimination using a simple, low-power DC glow discharge. This capability highlights its potential as a compact and complementary technique for rapid and *in situ* atomic isotopic analysis, extending the high-sensitivity capabilities of molecular CRDS to atomic spectroscopy. The method also holds potential for isotopic measurements of other rare-earth and transuranic elements, including uranium and plutonium, opening new opportunities for advanced isotopic analysis across diverse research fields.

Author contributions

Ryohei Terabayashi: conceptualization (supporting), Formal analysis (lead), project administration (supporting), investigation (lead), methodology (lead), software (lead), visualization (lead), funding acquisition (supporting), writing – original draft (lead). Yuko Nojiri: investigation (supporting), methodology (supporting), writing – review and editing (supporting), Shuichi Hasegawa: conceptualization (lead), funding acquisition (lead), project administration (lead), supervision (lead), writing – review and editing (lead).

Conflicts of interest

The authors have no conflicts to disclose.

Data availability

Data for this article are available at NAGOYA Repository (https://nagoya.repo.nii.ac.jp/records/2013631).

Acknowledgements

Part of this research was supported by the "HRD for Fukushima Daiichi Decommissioning based on Robotics and Nuclide Analysis," conducted under the Center of World Intelligence Project for Nuclear S&T and Human Resource Development by the Ministry of Education, Culture, Sports, Science and Technology (MEXT), Japan, and the JAEA Nuclear Energy S&T and Human Resource Development Project through the Concentrating Wisdom Grant (Grant Number JPJA18B18072148). This work was also supported by JSPS KAKENHI (Grant Number 23K13686).

References

1 G. Gagliardi and H. P. Loock, *Cavity-Enhanced Spectroscopy and Sensing*, Springer, 2014, DOI: 10.1007/978-3-642-40003-2.
2 G. Berden, *et al.*, Cavity ring-down spectroscopy: experimental schemes and applications, *Int. Rev. Phys. Chem.*, 2000, **19**, 565–607, DOI: 10.1080/014423500750040627.
3 S. S. Brown, *et al.*, Cavity ring-down spectroscopy for atmospheric trace gas detection: application to the nitrate radical (NO3), *Appl. Phys. B*, 2002, **75**, 173–182, DOI: 10.1007/s00340-002-0980-y.

4 E. R. Crosson, A cavity ring-down analyzer for measuring atmospheric levels of methane, carbon dioxide, and water vapor, *Appl. Phys. B*, 2008, **92**, 403–408, DOI: 10.1007/s00340-008-3135-y.
5 I. Galli, *et al.*, Spectroscopic detection of radiocarbon dioxide at parts-per-quadrillion sensitivity, *Optica*, 2016, **3**, 385–388, DOI: 10.1364/OPTICA.3.000385.
6 A. J. Fleisher, *et al.*, Optical measurement of radiocarbon below unity fraction modern by linear absorption spectroscopy, *J. Phys. Chem. Lett.*, 2017, **8**, 4550–4556, DOI: 10.1021/acs.jpclett.7b02105.
7 A. P. Yalin, *et al.*, Detection of sputtered metals with cavity ring-down spectroscopy, *Appl. Opt.*, 2005, **44**, 6496–6505, DOI: 10.1364/AO.44.006496.
8 W. Wei and A. Castro, Sensitive detection of an erbium isotope in an atomic beam using cavity ring-down spectroscopy, *Appl. Spectrosc.*, 2023, **78**, 120–124, DOI: 10.1177/00037028231211614.
9 C. Wang, Plasma-cavity ringdown spectroscopy (P-CRDS) for elemental and isotopic measurements, *J. Anal. At. Spectrom.*, 2007, **22**, 1347–1363, DOI: 10.1039/B701223C.
10 G. P. Miller and C. B. Winstead, Inductively Coupled Plasma Cavity Ringdown Spectrometry, *J. Anal. At. Spectrom.*, 1997, **12**, 907–912, DOI: 10.1039/A701523B.
11 C. Wang, *et al.*, Isotopic measurements of uranium using inductively coupled plasma cavity ringdown spectroscopy, *Appl. Spectrosc.*, 2003, **57**, 1167–1172, DOI: 10.1366/00037020360696044.
12 D. Ishikawa and S. Hasegawa, Hollow cathode atomic source applicable to gas, liquid residue, and solid sample phases, *J. Nucl. Sci. Technol.*, 2018, **56**, 809–813, DOI: 10.1080/00223131.2018.1532848.
13 D. Ishikawa and S. Hasegawa, Development of removable hollow cathode discharge apparatus for sputtering solid metals, *J. Spectrosc.*, 2019, **2019**, 491671, DOI: 10.1155/2019/7491671.
14 P. Jacquet, *et al.*, Cavity Ring-Down Spectroscopy for Gaseous Fission Products Trace Measurements in Sodium Fast Reactors, *IEEE Trans. Nucl. Sci.*, 2014, **61**, 2011–2016, DOI: 10.1109/TNS.2014.2304074.
15 J. Dumazert, *et al.*, Gadolinium for neutron detection in current nuclear instrumentation research: A review, *Nucl. Instrum. Methods Phys. Res., Sect. A*, 2018, **882**, 53–68, DOI: 10.1016/j.nima.2017.11.032.
16 R. Brennetot, *et al.*, Optimization of the operating conditions of a MC-ICP-MS for the isotopic analysis of gadolinium in spent nuclear fuel using experimental designs, *J. Anal. At. Spectrom.*, 2005, **20**, 500–507, DOI: 10.1039/B417967F.
17 H. Hidaka, *et al.*, High fluences of neutrons determined from Sm and Gd isotopic compositions in aubrites, *Earth Planet. Sci. Lett.*, 1999, **173**, 41–51, DOI: 10.1016/S0012-821X(99)00221-6.
18 H. Hidaka, Isotopic variations of Sm, Gd, Er and Yb found in planetary materials caused by neutron-capture reactions in nature, *J. Anal. Sci. Technol.*, 2024, **15**(14), 1–10, DOI: 10.1186/s40543-024-00424-6.
19 G. A. Miller, *et al.*, Gadolinium Neutron Capture Therapy, *Nucl. Technol.*, 1993, **103**, 320–331, DOI: 10.13182/NT93-A34855.
20 P. Sharma, *et al.*, Gd nanoparticulates: from magnetic resonance imaging to neutron capture therapy, *Adv. Powder Technol.*, 2007, **18**, 663–698, DOI: 10.1163/156855207782515030.
21 J. Chen, *et al.*, Gadolinium isotope separation by cation exchange chromatography, *J. Nucl. Sci. Technol.*, 1992, **29**, 1086–1092, DOI: 10.3327/jnst.29.1086.
22 A. Boda, *et al.*, Molecular modeling guided isotope separation of gadolinium with strong cation exchange resin using displacement chromatography, *Sep. Sci. Technol.*, 2017, **52**, 2300–2307, DOI: 10.1080/01496395.2016.1260141.
23 P. V. Kiran Kumar, *et al.*, Selective excitation of odd gadolinium isotopes using two-colour photoionisation schemes, *J. Nucl. Mater.*, 2000, **282**, 255–260, DOI: 10.1016/S0022-3115(00)00406-2.
24 H. Niki, *et al.*, Selectivity and Efficiency of Laser Isotope Separation Processes of Gadolinium, *J. Nucl. Sci. Technol.*, 2006, **43**, 427–431, DOI: 10.1080/18811248.2006.9711117.
25 H. Hidaka, *et al.*, Determination of the isotopic compositions of samarium and gadolinium by thermal ionization mass spectrometry, *Anal. Chem.*, 1995, **67**, 1437–1441, DOI: 10.1021/ac00104a021.
26 J. He, *et al.*, Determination of the isotopic composition of gadolinium using multicollector inductively coupled plasma mass spectrometry, *Anal. Chem.*, 2020, **92**, 6103–6110, DOI: 10.1021/acs.analchem.0c00531.
27 K. Blaum, *et al.*, High-resolution, three-step resonance ionization mass spectrometry of gadolinium, *AIP Conf. Proc.*, 2001, **584**, 141–144, DOI: 10.1063/1.1405595.
28 R. A. McFarlane, *et al.*, Single mode tuning dip in the power of an He-Ne optical maser, *Appl. Phys. Lett.*, 1963, **2**, 189–190, DOI: 10.1063/1.1753727.
29 G. Giusfredi, *et al.*, Theory of saturated-absorption cavity ring-down: radiocarbon dioxide detection, a case study, *J. Opt. Soc. Am. A*, 2015, **32**, 2223–2237, DOI: 10.1364/JOSAB.32.002223.
30 R. Aiello, *et al.*, Lamb-dip saturated-absorption cavity ring-down rovibrational molecular spectroscopy in the near-infrared, *Photonics Res.*, 2022, **10**, 1803–1809, DOI: 10.1364/PRJ.456515.
31 K. Fushimi, *et al.*, Saturated cavity ring-down spectroscopy of the Balmer-α line of atomic hydrogen for estimating sheath electric field in plasma, *J. Instrum.*, 2023, **18**, C10002, DOI: 10.1088/1748-0221/18/10/C10002.
32 P. Macko, *et al.*, A new model for the treatment of optical saturation for measuring Ne*($^3P_0$) metastable atoms density down to 1010 m^{-3} by cavity ring-down spectroscopy, *J. Phys. D: Appl. Phys.*, 2025, **58**, 385205, DOI: 10.1088/1361-6463/adfb8b.
33 A. O'Keefe, *et al.*, Cavity ring-down optical spectrometer for absorption measurements using pulsed laser sources, *Rev. Sci. Instrum.*, 1988, **59**, 2544–2551, DOI: 10.1063/1.1139895.

34 C. Wang, *et al.*, Cavity ringdown spectroscopy for diagnostic and analytical measurements in an inductively coupled plasma, *Appl. Spectrosc.*, 2002, **56**, 386–397, DOI: 10.1366/0003702021954773.
35 R. C. Hilborn, Einstein coefficients, cross sections, f values, dipole moments, and all that, *Am. J. Phys.*, 1982, **50**, 982–986, DOI: 10.1119/1.12937.
36 B. H. Armstrong, Spectrum line profiles: The Voigt function, *J. Quant. Spectrosc. Radiat. Transfer*, 1967, **7**, 61–88, DOI: 10.1016/0022-4073(67)90057-X.
37 R. W. Fox and L. Hollberg, Role of spurious reflections in ring-down spectroscopy, *Opt. Lett.*, 2002, **27**, 1833–1835, DOI: 10.1364/OL.27.001833.
38 W.-G. Jin, *et al.*, Hyperfine structure and isotope shift in high-lying levels of Gd I, *J. Phys. Soc. Jpn.*, 2011, **80**, 124301, DOI: 10.1143/JPSJ.80.124301.
39 I. Galli, *et al.*, Saturated-absorption cavity ring-down spectroscopy, *Phys. Rev. Lett.*, 2010, **104**, 110801, DOI: 10.1103/PhysRevLett.104.110801.
40 I. Sadiek and G. Friedrichs, Saturation dynamics and working limits of saturated absorption cavity ring-down spectroscopy, *Phys. Chem. Chem. Phys.*, 2016, **18**, 22978–22989, DOI: 10.1039/C6CP01966H.
41 Y. Iwata, *et al.*, Development of an interference-filter-type external-cavity diode laser for resonance ionization spectroscopy of strontium, *Rev. Sci. Instrum.*, 2019, **90**, 123002, DOI: 10.1063/1.5125307.
42 R. W. P. Drever, *et al.*, Laser phase and frequency stabilization using an optical resonator, *Appl. Phys. B*, 1983, **31**, 97–105, DOI: 10.1007/BF00702605.
43 M. Tarik, *et al.*, Development and fundamental investigation of laser ablation glow discharge time-of-flight mass spectrometry (LA-GD-TOFMS), *Spectrochim. Acta, Part B*, 2009, **64**, 262–270, DOI: 10.1016/j.sab.2009.02.009.
44 A. L. Gray, Solid sample introduction by laser ablation for inductively coupled plasma source mass spectrometry, *Analyst*, 1985, **110**, 551–556, DOI: 10.1039/AN9851000551.
45 J. Meija, *et al.*, Isotopic compositions of the elements 2013 (IUPAC Technical Report), *Pure Appl. Chem.*, 2016, **88**, 293–306, DOI: 10.1515/pac-2015-0503.
46 A. Kramida *et al.*, *NIST Atomic Spectra Database (Ver. 5.12)*, 2024, DOI: 10.18434/T4W30F.
47 K. Blaum, *et al.*, Isotope shifts and hyperfine structure in the [Xe]4f75d 6s2 9DJ → [Xe]4f75d 6s 6p 9FJ+1 transitions of gadolinium, *Eur. Phys. J. D*, 2000, **11**, 37–44, DOI: 10.1007/s100530070103.
48 J. B. Ko, New designs of glow discharge lamps for the analysis of metals by atomic emission spectroscopy, *Spectrochim. Acta, Part B*, 1984, **39**, 1405–1423, DOI: 10.1016/0584-8547(84)80221-9.